

Interface strength and degradation of adhesively bonded porous aluminum oxides

Abrahami, Shoshan; de Kok, John M.M.; Gudla, Visweswara C.; Ambat, Rajan; Terryn, Herman; Mol, Arjan

DOI

[10.1038/s41529-017-0007-0](https://doi.org/10.1038/s41529-017-0007-0)

Publication date

2017

Document Version

Final published version

Published in

npj Materials Degradation

Citation (APA)

Abrahami, S., de Kok, J. M. M., Gudla, V. C., Ambat, R., Terryn, H., & Mol, A. (2017). Interface strength and degradation of adhesively bonded porous aluminum oxides. *npj Materials Degradation*, 1, Article 8. <https://doi.org/10.1038/s41529-017-0007-0>

Important note

To cite this publication, please use the final published version (if applicable). Please check the document version above.

Copyright

Other than for strictly personal use, it is not permitted to download, forward or distribute the text or part of it, without the consent of the author(s) and/or copyright holder(s), unless the work is under an open content license such as Creative Commons.

Takedown policy

Please contact us and provide details if you believe this document breaches copyrights. We will remove access to the work immediately and investigate your claim.

ARTICLE OPEN

Interface strength and degradation of adhesively bonded porous aluminum oxides

Shoshan T. Abrahami^{1,2}, John M. M. de Kok³, Visweswara C. Gudla⁴, Rajan Ambat⁴, Herman Terryn^{2,5} and Johannes M. C. Mol^{1,2}

For more than six decades, chromic acid anodizing has been the main step in the surface treatment of aluminum for adhesively bonded aircraft structures. Soon this process, known for producing a readily adherent oxide with an excellent corrosion resistance, will be banned by strict international environmental and health regulations. Replacing this traditional process in a high-demanding and high-risk industry such as aircraft construction requires an in-depth understanding of the underlying adhesion and degradation mechanisms at the oxide/resin interface resulting from alternative processes. The relationship between the anodizing conditions in sulfuric and mixtures of sulfuric and phosphoric acid electrolytes and the formation and durability of bonding under various environmental conditions was investigated. Scanning electron microscopy was used to characterize the oxide features. Selected specimens were studied with transmission electron microscopy coupled with energy-dispersive X-ray spectroscopy to measure resin concentration within structurally different porous anodic oxide layers as a function of depth. Results show that there are two critical morphological aspects for strong and durable bonding. First, a minimum pore size is pivotal for the formation of a stable interface, as reflected by the initial peel strengths. Second, the increased surface roughness of the oxide/resin interface caused by extended chemical dissolution at higher temperature and higher phosphoric acid concentration is crucial to assure bond durability under water ingress. There is, however, an upper limit to the beneficial amount of anodic dissolution above which bonds are prone for corrosive degradation. Morphology is, however, not the only prerequisite for good bonding and bond performance also depends on the oxides' chemical composition.

npj Materials Degradation (2017)1:8; doi:10.1038/s41529-017-0007-0

INTRODUCTION

Long-term service of adhesively bonded aircraft structures relies upon the durability of adhesion between the aluminum substrates and the adhesive. The importance of surface preparation for bond durability was recognized in the early days of the aerospace industry. Initially, pre-treatments for structural bonding included only chemical degreasing and etching using Cr(VI)-based solutions.¹ This combination was sufficient to primarily remove the mechanically weak surface layers, including the native oxide, and subsequently produce a new micro-rough surface oxide that is suitable for adhesion. Later on, anodizing was added to the pre-treatment procedure, mainly to increase overall corrosion resistance.² Utilizing low pH electrolytes for anodic oxidation produces a porous self-ordered hexagonal oxide structure on top of a compact barrier layer.³ The anodic oxidation is driven by an external voltage or current source. Hence, the oxide films produced by this method can be substantially thicker than those obtained using chemical etching.

Over the years, industrial and scientific research has greatly contributed to our understanding of the changes that take place during surface treatments of aluminum and its alloys, as well as the influence of different processing parameters.⁴ Nevertheless, the excellent adhesion and corrosion resistance that is achieved by the complete Cr(VI)-based pre-treatment process currently

applied by the European aerospace industry is not easily duplicated.⁵ Since strict international environmental and health regulations announced the near future ban of Cr(VI), its replacement has become a critical and timely issue.⁶ Reviewing the literature to date, the high strength of these bonded structures is attributed to the accumulated effect of two main mechanisms: (1) mechanical interlocking and (2) chemical interactions and physical interactions between the oxide and the organic resin.^{7–9} However, their extent and role remains unclear.

Since candidate Cr(VI)-free electrolytes such as sulfuric acid (SAA) and phosphoric-sulfuric acid (PSA) mixtures introduce different chemical and morphological modifications in comparison to the oxide produced by chromic acid anodizing, their effects on adhesion strength and durability are not well understood. In our previous study, we reported that the density of hydroxyl species at the surface of the oxide is closely related to the stability of bonding with an epoxy-based adhesive upon the ingress of water.¹⁰ Since the former study has been conducted on thin, featureless barrier anodic oxide films, it does not take into account variations in the surface roughness that can lead to different levels of mechanical interlocking. Hence, in this study we explore the additional effect of changes in the oxide morphology on the resulting adhesion strength and stability. To this aim, a set of samples with anodic films having a range of pore sizes and

¹Materials Innovation Institute (M2i), Elektronicaweg 25, Delft, 2628 XG, The Netherlands; ²Department of Materials Science and Engineering, Delft University of Technology, Mekelweg 2, 2628 CD Delft, The Netherlands; ³Fokker Aerostructures BV, Industrieweg 4, 3351 LB Papendrecht, The Netherlands; ⁴Section of Materials and Surface Engineering, Department of Mechanical Engineering, Technical University of Denmark, Kongens Lyngby 2800, Denmark and ⁵Department of Materials and Chemistry, Research Group Electrochemical and Surface Engineering (SURF), Vrije Universiteit Brussel, Pleinlaan 2, 1050 Brussels, Belgium
Correspondence: Johannes M. C. Mol (J.M.C.Mol@tudelft.nl)

Received: 23 December 2016 Revised: 6 January 2017 Accepted: 23 January 2017

Published online: 21 August 2017

lengths were prepared and characterized. The penetration of the resin into the various oxide pores was studied using high-resolution scanning and transmission electron microscopy (TEM) coupled with energy-dispersive X-ray spectroscopy (EDS) and related to its resulting bonding performance measured using floating roller peel tests.

RESULTS

Oxide film morphology

Film thickness and surface morphology. The diverse anodizing conditions that were applied in this study resulted in porous oxide layers with a broad range of morphological features and dimensions. Scanning electron microscopy (SEM) measurements were used to determine the oxide thickness and pore size. Pore diameter (measured at the surface) ranges between 5 and 60 nm, with varying oxide film thicknesses of up to 6 μm . A full list of the anodizing conditions and measurements is given in Supplementary Table S1 in the supporting information. The general trends are highlighted below.

Top view SEM images of selected oxides are shown in Fig. 1. The corresponding anodizing conditions and measured pore thickness and oxide thickness are listed in Table 1. A clear change in the morphology as a function of the anodizing conditions is visible. The pore size of the different oxides is generally visible in the images at high magnification. The SAA oxides at both 20 and 50 $^{\circ}\text{C}$ produce a relatively dense honeycomb porous structure with finer pores for the lower anodizing temperature (Fig. 1a and b for SAA20 and SAA50, respectively). Since except for the temperature the anodizing conditions are similar, pore widening is caused by

the prolonged contact with the high-temperature electrolyte. When the anodizing electrolyte also contained phosphoric acid, pores were already wider at 20 $^{\circ}\text{C}$ (Fig. 1c). Finally, more aggressive anodizing conditions that include phosphoric acid and higher temperatures cause such extended dissolution that collapses the top part of the oxide during anodizing, exhibiting a “bird’s nest”-like structure on top of the honeycomb (Fig. 1d and e for PSA35 and PSA50, respectively). These additional features significantly increase the surface roughness of these oxides. This is noticeable in the images taken at lower magnifications. “Bird’s nests” that extend between 0.5 and 2 μm in lateral size on PSA35 and PSA50 provide an extra microscopic roughness to the oxide surface. Since these “nests” are clusters of nano-sized ridges and pore walls, they also provide a nano-roughness that significantly increases the effective surface area. Conversely, the top surface of both SAA oxides and PSA20 that do not exhibit these features are relatively smooth (Fig. 1a–c).

In addition to the electrolyte composition and temperature, variations in the voltage and anodizing time were also found to affect the morphology of the produced anodic oxides. Pore size at the surface generally becomes larger with time due to the extended period of contact with the dissolving electrolyte. The higher the anodizing temperature and the concentration of phosphoric acid, the larger the difference in pore size for short (15 min) and long (30 min) anodizing times. Similar trends were observed when a higher anodizing voltage was applied.

The extent of oxide dissolution can be deduced by comparing the accumulated charge density, Q (calculated from the measured current density and the time that passed during anodizing) and the final oxide thickness. The higher the anodizing temperature,

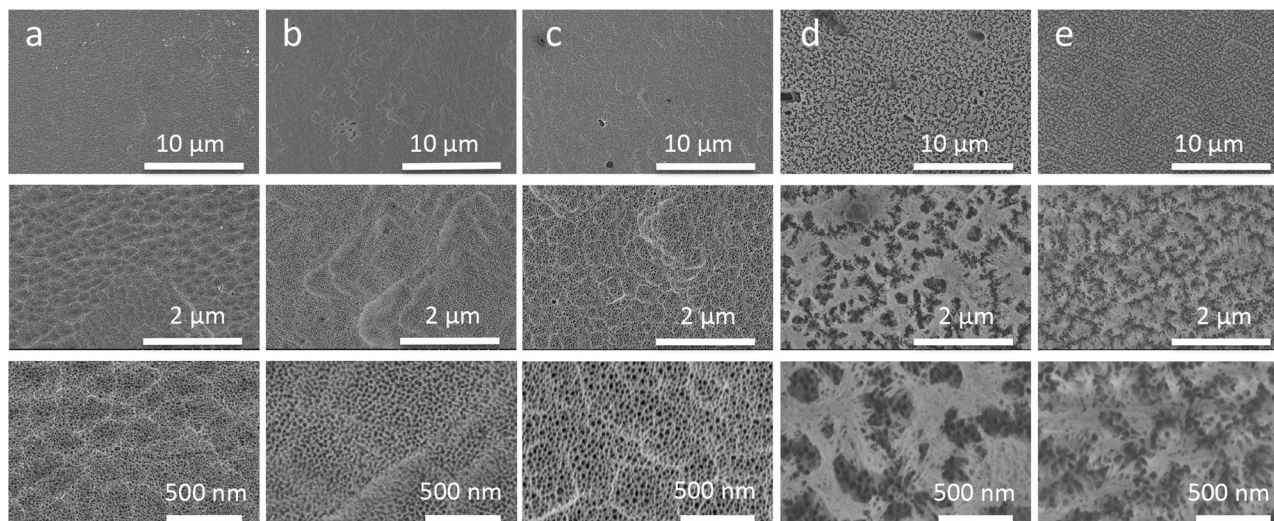


Fig. 1 Secondary electron SEM images of the surface morphology of anodic oxides produced by anodizing in: **a** SAA20, **b** SAA50, **c** PSA20, **d** PSA35, and **e** PSA50 (full experimental conditions are listed in Supplementary Table S1)

Table 1. Anodizing conditions and measured oxide features (TEM) for the selected samples shown in Figs. 1 and 2

Abbreviation	H ₂ SO ₄ (g/l)	H ₃ PO ₄ (g/l)	Voltage (V)	Anodizing time (min)	Oxide thickness (μm)	Pore diameter (nm) (Top)	Pore diameter (nm) (Bottom)	Barrier-layer thickness (nm)
SAA20	10	0	19	30	1.2 \pm 0.1	8 \pm 4	13 \pm 4	15 \pm 2
SAA50	10	0	19	30	5.0 \pm 0.4	22 \pm 3	8 \pm 2	17 \pm 2
PSA20	10	80	26	15	0.7 \pm 0.1	22 \pm 5	25 \pm 3	30 \pm 2
PSA35	50	80	19	30	3.0 \pm 0.4	28 \pm 5	15 \pm 5	20 \pm 4
PSA50	10	40	23	15	1.6 \pm 0.6	30 \pm 4	20 \pm 3	26 \pm 3

the more the oxide thickness deviates from the linear relationship that is predicted using Faraday's law of electrolysis (the *solid line* in Supplementary Fig. S1). In addition, this deviation is more prominent for higher phosphoric acid concentrations (not indicated).

High-resolution oxide morphology

Five different panels that were produced by varying anodizing conditions had been chosen for a detailed study using high-resolution TEM. To investigate the interface area, lamellas were prepared using focused ion beam (FIB) milling from cross-sections of the samples. Supplementary Figure S2 shows an example of such cross-section. Also visible in Supplementary Fig. S2 is the border between the primer and the adhesive layer. Primers are commonly used to seal the oxide immediately after the pre-treatment (and before bonding) for protection. Since they are diluted versions of the adhesives, it is generally also presumed that they can penetrate more easily into the pores, assisting in the formation of a stable bonding. From here on, the primer and adhesive are generally referred to as the resin.

High-resolution TEM bright field images of the five chosen oxides are shown in Fig. 2. Both SAA20 and PSA20 oxides (Fig. 2b and f) show a branched morphology with similar features throughout the oxide film thickness and a relatively smooth oxide/resin interface. Some branching with undeveloped pores can be distinguished at the surface of these oxides. This indicates of a very limited chemical dissolution during anodizing, since the "history" of the initial pore development stages is still present. Conversely, the advanced dissolution of the films prepared at 35 and 50 °C (Fig. 2d, h, j), resulted in oxides that are much rougher, irregular, and thinned at the oxide/resin interface. Although a relatively high anodizing temperature leads to widening of the pores at the oxide/resin interface, it seems to have little to no effect on the features in the interior of the oxide. The "birds nest" morphology that was previously observed in Fig. 1d and e can be distinguished in the cross-section view of the corresponding oxides (Fig. 2h, j). They display a "zigzag" morphology at the upper part of the oxide. Although not visible in the SEM image in Fig. 1b, similar features could be seen on the SAA50 oxide, but at a much lower extent and density (for an example, see Supplementary Fig. S3 in the supporting information). Hence, an additional micro- and nano-roughness is present at the surface of the high-temperature oxides, the extent of which is seen to vary with the temperature and/or phosphoric acid concentration.

Table 1 lists the measured morphological features that were retrieved from the TEM images in Fig. 2. Under the concentration and potential conditions, as in SAA20 and SAA50, the oxide thickness increases with an increasing anodizing temperature, in accordance with Schneider et al.¹¹ The thickness of the barrier layer generally corresponds to the applied voltage following the 1.2 nm/V relation.⁴ The relation accurately predicts the barrier-layer thickness of both SAA oxides, while the measured values for PSA oxides are slightly larger than expected. Pore diameters for 20 °C oxides do not differ much at bottom and top part of the oxide. For 35 and 50 °C anodizing, pores are much larger at the surface due to chemical dissolution.

Resin penetration

It is also important to relate the oxide geometrical features to the extent at which the resin is able to penetrate into the oxide. Figure 2 displays the concentration profiles of the main elements detected by TEM-EDS measurements on the corresponding lamellas. The three different phases: aluminum (A), oxide (O), and resin (R) can be clearly distinguished. Except for copper that arises from the TEM sample holder (and is detected in all cases), only Al is found in the substrate region.

Some sulfur and phosphorus were detected in the relevant oxides that mainly consisted of aluminum and oxygen. These arise from the incorporation of anions during anodizing in the corresponding acids and their concentration correspond to the levels previously measured by AES on barrier-type oxides.¹² Sulfur (1–3 wt.%) was detected throughout the SAA oxides and 0.0–1.0 wt.% phosphorus and 0.0–2.0 wt.% of sulfur were detected in the PSA oxides.

The organic-based resin is mostly composed of carbon and oxygen, with inorganic additives such as silicon and bromine. Because some degree of carbon contamination is expected on all anodic oxides due to ambient exposure before bonding (as well as lamella processing),¹³ the most definite indicators for the presence of resin in the pores are silicon and bromine. Silicon was found mostly close to the oxide/resin interface of all specimens. Its presence suggests that silane adhesion promoters may have been incorporated into the primer chemistry. Bromine was detected in all specimens, with an initial concentration of 0.1 wt.% at the oxide/resin interface and increasingly higher concentration toward the bulk of the resin. Maximal detected concentration of bromine ranged from 5 to 12 wt.%. Although these two elements are definite indications for the presence of resin within the oxide, their concentration is very low (especially for Si, with 0.1–0.2 wt. %). Moreover, bromine concentration profiles in Fig. 2 generally follow the same trend as the corresponding carbon profile. Carbon is therefore further used as a measure for the presence of resin within the oxides.

Comparing the different profiles show that the carbon content in the bulk of the resin is similar in all specimens, ranging between 60 and 80 wt.% C. At the resin/oxide interface, however, differences start to emerge. For PSA35 and PSA50 oxides, carbon concentration decreases gradually until it reaches a minimum of 6–18 wt.% near the bottom of the oxide. Conversely, the carbon concentration drops abruptly at the oxide/resin interface of SAA20, SAA50, and PSA20 oxides. This observation can be assigned to differences in surface roughness at the oxide/resin interface. The presence of "bird's nests" at the interface leads to an extended transition zone.

Pore size appears to play a role in determining the amount of resin penetration. PSA oxides that have a larger pore size near the oxide/aluminum interface display relatively high carbon concentration. Conversely, the carbon concentration within SAA oxides drops to a minimum value of 1–2 wt.% near the bottom of the oxide. This minimum concentration is significantly lower than the final carbon concentration that was detected in PSA oxides (6–18 wt.%).

Mechanical performance

Since the Floating roller peel test (shown in Fig. 3e simulates the most severe type of loading on the assembly (mode I/II), it is used to evaluate the lower limit of adhesion strength.¹⁴ When tested under dry conditions, it measures the quality of the initial bonding. Under wet conditions, bond durability is tested, as water ingress is often cited as the main cause for environmental adhesion failure.¹⁵ Figure 3a and b displays the measured dry peel strength vs. the pore diameters and the oxide thickness, respectively. It shows that, up to a certain limit, the initial peel strength increases with the pore size. Almost all oxides with pore diameters >15 nm fulfill the minimum level of strength (300 N) with required cohesive fracture (shown in Fig. 3g). Above ~25 nm, the dry peel strength remains relatively constant and independent of the pore size. There is, on the other hand, no correlation between oxide thickness and its dry peel strength (Fig. 3b).

Figure 3c and d indicate the trends in the measured wet peel strength vs. the pore diameters and the oxide thickness, respectively. In contrast to the previous results, the wet peel strengths display no clear relation to the pore size. It is interesting

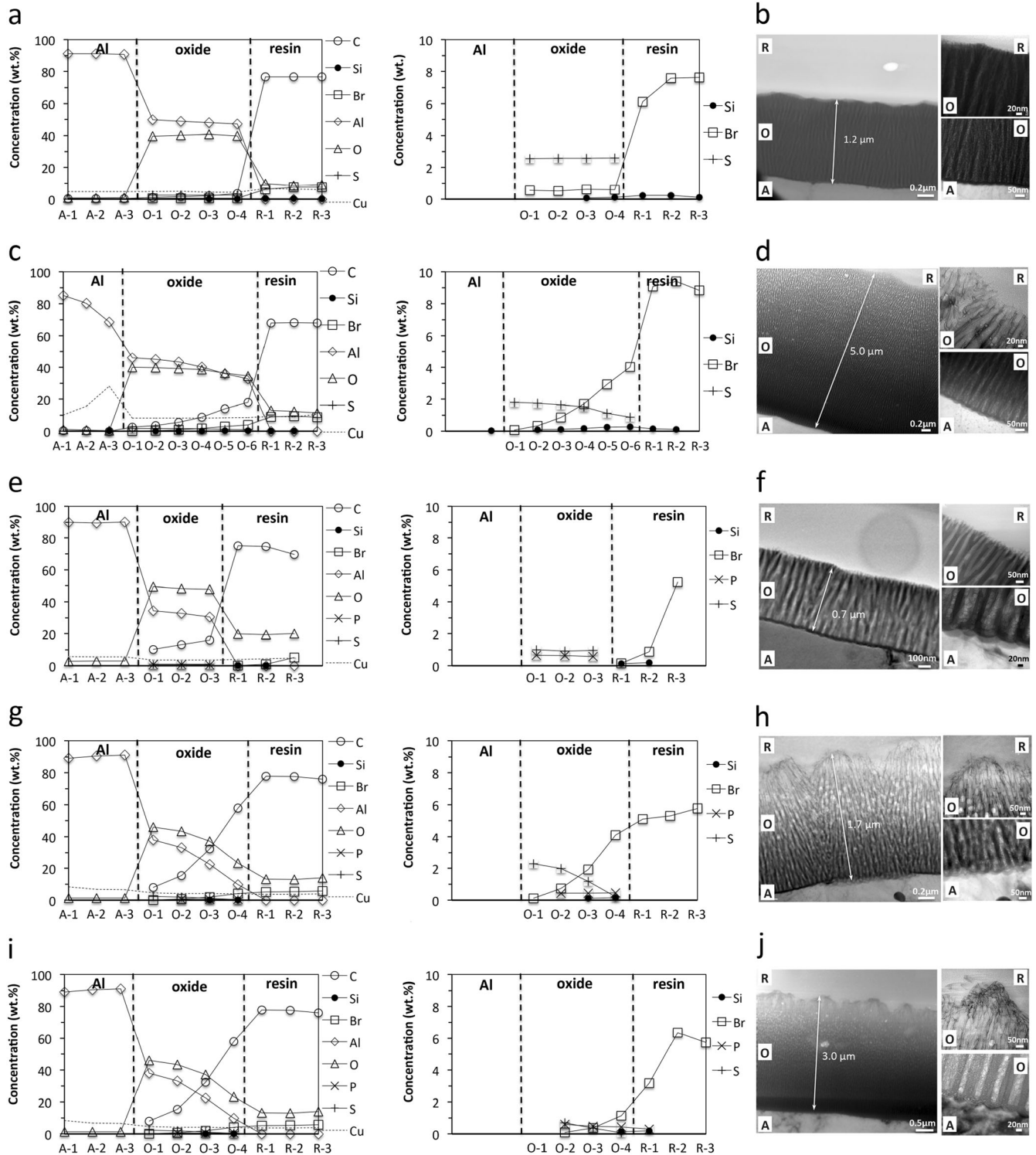


Fig. 2 TEM-EDS concentration profiles (*left column*) and a closer look at selected low-concentration elements (*middle column*). Notice that due to differences in oxide thickness, the last measurements within an oxide, as well as the distance within two points differ between specimens. On the *right*: the corresponding bright field TEM micrographs of the five selected oxides. For each TEM image: a complete cross-section (*large*) and zoom-in at the top and bottom part of the oxide (*smaller images*) are shown. Anodizing conditions: **a, b** SAA20, **c, d** SAA50, **e, f** PSA20, **g, h** PSA35, and **i, j** PSA50

to note that oxides with similar pore size (at the surface) showed different mechanical performance depending on the electrolyte combination and temperature. A clear distinction is made between anodizing at 20 and 50 $^{\circ}\text{C}$. Besides a single exception (that involves the highest phosphoric acid concentration), all the

oxides produced at 20 $^{\circ}\text{C}$ underperform. Oxides produced at 50 $^{\circ}\text{C}$ show higher strength values than the average. This trend is also reflected in the five selected oxides in Table 2. The performance of oxides prepared at 35 $^{\circ}\text{C}$ varied according to the combination of the preparation conditions. Also under wet conditions, no

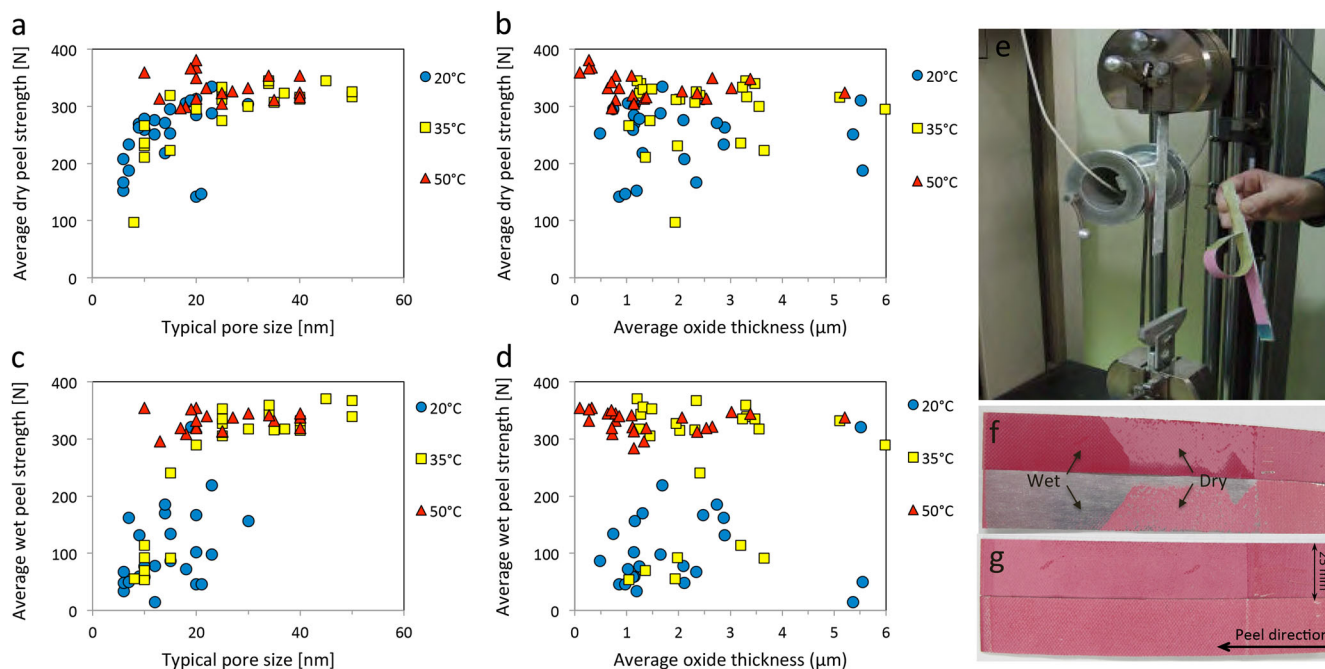


Fig. 3 Average dry peel strength vs. the average oxide pore diameter (**a**) and the average oxide thickness (**b**). Average wet peel strength vs. the pore diameters (**c**) and the average oxide thickness (**d**), both determined by SEM. Floating roller peel test set-up (**e**) and typical failure modes of panels after testing. Oxide preparation conditions SAA20 (**f**) and SAA50 (**g**)

Table 2. Summary of the mechanical performance of the selected oxides

Abbreviation	Floating roller peel		Average dry peel after SST		Average bondline corrosion	
	Dry peel (N)	Wet peel (N)	90 days (N)	180 days (N)	90 days (%)	180 days (%)
SAA20C	153	33	n.a.	17	85	93
SAA50C	324	338	335	336	3	3
PSA20C	147	46	n.a.	19	75	95
PSA35C	333	335	308	315	4	1
PSA50C	326	338	333	299	5	21

correlation was found between the anodic oxide thickness and the measured peel strength (Fig. 3d).

Generally, the wet peel strength of oxides prepared at 20 °C is much lower than their dry peel strength; while they exhibited an interface (adhesive) failure in the presence of water (e.g., in Fig. 3f). Oxides with similar pore size, but prepared at higher anodizing temperature perform better. The wet peel strength of these panels is slightly higher than the dry peel test and they exhibited cohesive failure throughout the entire panel (e.g., in Fig. 3g).

Bondline corrosion

Another way to test the durability of the bond is by exposing it to harsh environmental conditions, i.e., by placing the bonded panels in a salt spray cabinet. This test was undertaken in here for 90 and 180 days. The level of corrosion on the different panels was visually inspected after each exposure period. The complete list of the results can be found in Supplementary Table S1 in the supporting material and in Table 2 for the selected specimens. Examples of highly corroded and corrosion-resistant panels are shown in Fig. 4b and c for SAA 20 °C and SAA 50 °C, respectively.

In addition, post-exposure (dry) peel strengths were measured. As illustrated in Fig. 4a, there is an almost linear correlation between the amount of corrosion measured on a panel and the reduction of its peel strength. There is also a high correspondence

with the anodizing temperature, but it is apparently not the only critical factor. Further, anodizing at 20 °C generally results in the worst performance. The only exception is the oxide produced at the highest concentration of phosphoric acid and anodized for 30 min at higher voltage. In contrast to the previous results, few of the 50 °C oxides exhibited very poor mechanical performance. The observed level of performance for these oxides within each electrolyte mixture can be roughly classified as “good” for high voltage and “poor” for low voltage. However, there is no correlation to the value of the anodizing voltage itself. Most SAA and 20 °C PSA oxides performed poorly, even at relatively high voltages (Supplementary Table S1). Oxides prepared at 35 °C generally performed well when prepared at higher acid concentrations. These results suggest a link to the amount of dissolution of the anodic oxide by the anodizing electrolyte. Dissolution of the oxide to a certain extent seem to be beneficial, while too much of it, which may be beneficial in terms of bonding, is detrimental for the corrosion resistance.

Supplementary Figure S4 shows a comparison between the average peel strength after 180 days in the salt spray cabinet and the dry peel and wet peel strength of the “fresh” joint. As seen in the figure, there is no clear correlation between the different tests, but severity of the tests can be ranked in the following order: bondline corrosion > wet peel > dry peel. Panels that passed in

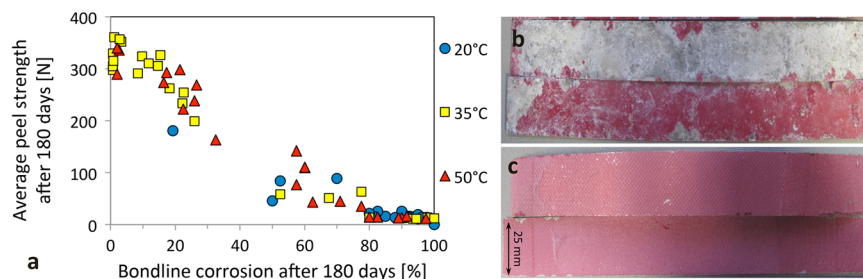


Fig. 4 **a** Left: Average peel strength after 180 days in the salt spray cabinet vs. the amount of bondline corrosion. **Right:** Characteristic images of the peeled panels that represented poor (**b**) and good adhesion (**c**). Oxide preparation conditions **b** SAA20 and SAA50 **c**

peel after a bondline corrosion test also passed the other two tests.

DISCUSSION

The results in this study demonstrate that the anodizing conditions are crucial in determining the adhesive bond strength and durability. Overall, the most dominant parameters that determine the final morphology of the oxide are the electrolyte composition and the anodizing temperature. In accordance with the geometrical model that was developed by Keller et al.,¹⁶ the structural dimensions are determined by the applied voltage and the nature of the electrolyte. In this study, we show that the electrolyte temperature also plays an important role. In contrast to the addition of phosphoric acid, a high electrolyte temperature does not change the pore diameter close to the metal/oxide interface, which is determined by the applied voltage.¹⁷ The higher temperature only widens the pore openings at the surface through chemical dissolution. Since the top part of the oxide is in contact with the acid for a longer period of time, it is much more affected than the interior. The resulted difference in morphology as a result of increasing the anodizing temperature is illustrated in Fig. 5b. As discussed for the case of SAA20 vs. SAA50, this can make the difference between the mechanical performances of the bond joints.

Owing to the considerable “dissolving action” of H_3PO_4 , the pore size of PSA oxides is larger than for SAA oxides. Varying the acid concentration and the anodizing conditions (voltage, time, and electrolyte temperature) can then be used to further modify the oxide morphology. This is reflected in the geometrical features, as measured by SEM and TEM. Moreover, these images reveal that changing the anodizing conditions also influences the surface roughness. A difference is then created between the relatively smooth top surface of porous oxides that are produced at lower temperatures and the micro- and nano-rough surfaces that are produced at higher electrolyte temperatures and phosphoric acid concentration.

Mechanical tests revealed that good initial bonding between the substrate and the resin is achieved as long as the pore size exceeds a critical threshold of about 20 nm. TEM-EDS measurements indicate that these performance differences correspond to the extent in which the resin is able to fill the pores. Narrow pores that are only partly filled with the resin provide a very limited contact between the oxide and the resin. In such cases, the contact area between the two phases and the loading mode are more similar to featureless oxides, as illustrated in Fig. 5c. The peel strength for such featureless oxides with an epoxy adhesive was previously reported in Abrahami et al.¹⁰ Their dry peel strength was in the same order of magnitude as porous oxides with small pores shown here. Once the pores are large enough and the resin penetrates into the pores, sufficient bonding is achieved and no further improvements in peel strength are registered. It can be argued that completely filled pores enhance the two main adhesion mechanisms: (1) it facilitates mechanical interlocking

and (2) it provides a larger surface area for interfacial interactions between the oxide and the resin. From a purely mechanical perspective, the fact that the contact angle between the oxide and the resin is constantly changing with respect to the direction of the exerted force already gives it an advantage over smooth surfaces or incompletely filled pores (Fig. 5c).

In contrast to dry conditions; the anodizing temperature rather than the pore size, considerably influences the peel strength under the ingress of water. These results agrees with earlier findings by Rider and Arnott¹⁸ using ultra-milling for surface roughening. The nanoscale protrusions and microscopic “bird’s nests” that are formed during high temperature anodizing produces a complex surface topography that hinders water diffusion. Also in the absence of surface roughness, a higher anodizing temperature was found to increase interface bond stability in the presence of water.¹⁰ This can be related to changes in the chemical properties of the oxide.¹⁹

Unexpected observation concerns the fact that dry and wet peel strengths are independent of the oxide thickness. It appears that the amount of contact area between the oxide and the resin is less important than the fact that a fully cohesive interphase is formed. This has previously been explained by Kinloch et al.²⁰ by the susceptibility of incompletely filled pores to an attack by water. Moreover, this observation confirms earlier findings by Venables et al.,²¹ who noticed that adhesion improvements are already provided by the whisker-like protrusions of the Forest products laboratory etch of just a few tens of nanometers long. The “bird’s nest” morphology in this study provides an extended version of this whiskers protrusions. A recent study by Ye et al.²² and Jeong and Choi²³ found the “birds nest” morphology to be superhydrophilic. Hence, the presence of surface roughness on porous oxide provides an extra advantage toward the smoother porous oxides that were prepared at lower temperatures. Comparing the carbon profiles near the oxide/resin interface, the advantage of a high surface roughness is visible by the more gradual and extended transition. Upon contact with the resin, a rough surface oxide extends the interphase to a three-dimensional resin/oxide composite.

There is, however, an upper limit to the beneficial amount of anodic dissolution, above which it negatively affects the resistance to bondline corrosion. This was found to be the most critical factor in determining the long-term performance of the joints in this study. The fact that bondline corrosion failure occurred at high-temperature oxides that were prepared at lower forming voltages, is possibly associated to the barrier-layer thickness.¹⁷ However, further electrochemical studies are needed for confirmation.

It is however also clear from the results that morphology is not the only prerequisite for good bonding. Although the carbon concentration close to the oxide/resin interface of SAA50 is approximately four times higher than for SAA20 (Fig. 2: (c) O-6 vs. (a) O-4), it is almost as low as for PSA20 (Fig. 2e O-3), while the two exhibit very different mechanical performance. In our earlier study it was reported that interfacial bonding between anodic oxides and epoxy resin proceeds through the hydroxyl groups at the

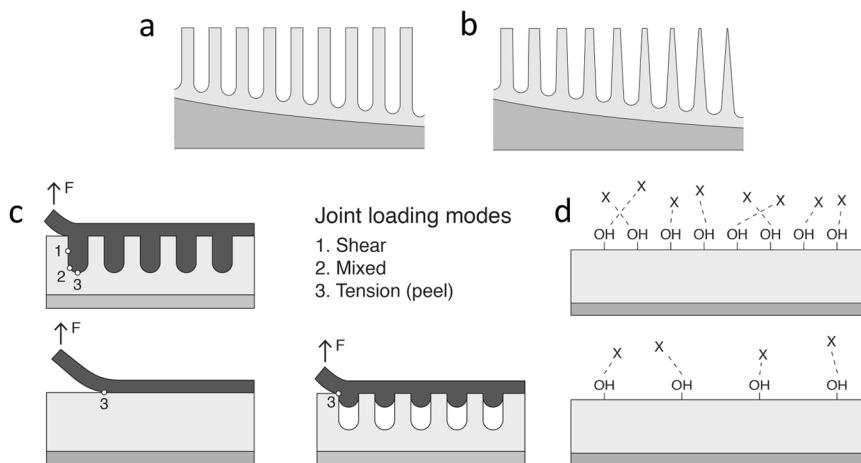


Fig. 5 Schematic illustrations of: the effect of anodizing temperature on the oxide morphology, for 20 °C (**a**) 50 °C (**b**), a comparison between pores, the extent of resin penetration and its effect on the contact area and the mechanical advantage provided by completely filled pores and a larger contact area (**c**) and the effect of hydroxyl density on interfacial bonding with adhesive (represented by *x*) (**d**)

surface of the oxide.¹⁰ The incorporation of phosphate and sulfate anions did not change the bonding mechanism; it only affected the amount of hydroxyl groups available for bonding. It was found that the density of hydroxyl groups at the surface of SAA oxide is larger than for PSA oxides (approximately double, depending on the anodizing conditions).¹² Therefore, higher peel strengths can be achieved with less surface area and performance differences can be related to changes in the oxide chemistry, as illustrated in Fig. 5d. Since phosphates and sulfates at the surface did not appear to contribute to bonding, they are not included in the illustration.

In summary, the results in this study demonstrate that the anodizing conditions, especially temperature and phosphoric acid concentration, are significantly affecting the morphology of the anodic oxides. Morphological changes were distinguished between geometrical modifications that affect the pore size and changes in the surface roughness that was caused by extended chemical dissolution. It was shown using TEM-EDS that resin penetration is affected by both morphological aspects. Consequentially, bond strength and durability is closely related to oxide morphology. Additionally, this study demonstrates that the overall bond performance of aluminum joints is a delicate and complex interplay between oxide surface morphology as well as oxide chemistry. Both adhesion mechanisms; adsorption and mechanical interlocking, contribute to the adhesion in these structural bonds. This study provides crucial insights into the relation between the anodizing conditions, the oxide morphology and resulting adhesion properties, which is of pivotal importance in the design and development of optimal Cr(VI)-free anodizing processes for aerospace adhesive bonding. Overall, the results illustrate the need to consider both chemical and morphological changes in the selection of Cr(VI)-free alternatives for a strong and durable adhesive bonding.

METHODS

Materials and sample preparation

The effect of anodizing conditions was studied on an AA7075-T6 alclad (clad layer AA7072). Six different combinations of phosphoric acid (H_3PO_4) and/or sulfuric acid (H_2SO_4) concentrations were used, as presented in Supplementary Table S1. Within each electrolyte combination, three different parameters were varied: temperature (20, 35, and 50 °C), anodizing dwell time (15 and 30 min) and voltage (preselected to yield a stable process at “low” and “high” relative voltages, see supporting information for the exact values, since they varied with the electrolyte and the anodizing conditions).

Prior to anodizing, all specimens were degreased in 50 g/l Metaclean T2001/4 VP2 (Chemie-Vertrieb GmbH) at 67.5 °C for 15 min. This was followed by etching in 35 g/l P3 Almecco (Henkel) for ~5 min at 35 °C for 3–4 μm metal removal and desmuting in 150 g/l Desoxin AL (Enthone) for 15 min at 30 °C. After anodizing the panels were dried at 45 °C for 30 min.

Panels for mechanical testing were additionally coated with 1–2 μm of phenol formaldehyde primer layer (Redux 101, Hexel, without inhibitor) and an AF163 epoxy structural adhesive film (3 M). All panels were bonded at 6 bar and cured at 125 °C for 75 min.

Floating roller peel tests were performed according to ASTM D3167-03a.²⁴ The panels were cut into 25 mm wide samples using a lint saw. After fixing the test panels in the apparatus, the unbound end of the specimen was attached to the lower head of the testing machine. The thin panel was peeled off the thicker panel at a speed of 100 mm/min. The peeling load vs. head movement (or load vs. distance peeled) was recorded. All tests were performed at ambient temperature. The first half of the specimen was peeled under dry (atmospheric) conditions. Water containing surfactants were then applied to the crack-tip and the second half was peeled under wet conditions.

Additional bonded panels were placed in a salt cabinet for accelerated corrosion testing using the standard conditions (ISO 9227) for the neutral salt spray test. After 90 and 180 days of exposure, panels were tested for (dry) peel strength and visually examined for the extent of bondline corrosion.

Scanning electron microscopy

Pore size and oxide thickness were measured from top- and cross-section view using Hitachi SEM SU-70. Image capturing occurred at an accelerating voltage of 2.0 keV, a current of 19–20 μA and a working distance of 2.0–3.4 mm. No Pt coating was applied. The image software system AnalySIS was used to measure pore and interpore distances close to the outer surface and close to the barrier layer.

A cross-section of selected panels was cut using a diamond saw and (cold) embedded. The cross-sections were then grinded and polished down to 1 μm using a diamond paste. Lamellas for TEM measurements were then prepared from the by focused ion beam (Helios Nanolab 600, Dual Beam FEI) milling and in situ lift out from the interface of the adhesive joint. The lamellas of ~1 μm thick were further thinned down for electron transparency to an approximate thickness of 120 nm and low energy milling (2 keV) was finally performed to remove any ion beam induced artifacts and damage to the samples.

Transmission electron microscopy

Selected panels were chosen for detailed microstructural characterization using a transmission electron microscope (Tecnai T20 G2, FEI) operating at 200 keV. The local composition of the anodic oxide and the relative concentrations of the resin in the porous structure were measured using an X-ray EDS (Oxford X-Max SDD X-ray detector) coupled to the TEM.

ACKNOWLEDGMENTS

This research was carried out under the project number M11.6.12473 in the framework of the Research Program of the Materials innovation institute M2i (www.m2i.nl). The paper contains results that were obtained by the industrial partner Fokker Aerostructures that are published within the collaboration on this project. We also thank M. Pen for his help with making the illustrations.

AUTHOR CONTRIBUTIONS

S.A., J.K., H.T. and J.M. were responsible for conception and design of the study. Fokker Aerostructures commissioned the SEM and peel tests. Analysis and interpretation of this data were completed by S.A., J.K., H.T. and J.M.. FIB lift out, TEM and TEM-EDS data were collected by V.G. and S.A., under the supervision of R.A.. S.T. drafted the article, while all coauthors contributed to the scientific and textual content by critical revision and editing. Final approval of the version to be published was given by all authors.

ADDITIONAL INFORMATION

Supplementary Information accompanies the paper on the *npj Materials Degradation* website (doi:[10.1038/s41529-017-0007-0](https://doi.org/10.1038/s41529-017-0007-0)).

Competing interests: The authors declare that they have no competing financial interests.

Publisher's note: Springer Nature remains neutral with regard to jurisdictional claims in published maps and institutional affiliations.

REFERENCES

1. Wegman, R. F. & Van Twisk, J. in *Surface Preparation Techniques for Adhesive Bonding* 2nd edn (eds Wegman, R. F. & Van Twisk, J.) Ch. 2, (William Andrew Publishing, 2013).
2. Higgins, A. Adhesive bonding of aircraft structures. *Int. J. Adhes. Adhes.* **20**, 367–376 (2000).
3. Sheasby, P. G. & Pinner, R. *Surface Treatment and Finishing of Aluminium and its Alloys* 6th edn (Finishing Publications Ltd., 2001).
4. Sulka, G. D. in *Nanostructured Materials in Electrochemistry* (ed Eftekhari, A.) Ch. 1 (Wiley-VCH Verlag GmbH & Co. KGaA, 2008).
5. Critchlow, G. W., Yendall, K. A., Bahrani, D., Quinn, A. & Andrews, F. Strategies for the replacement of chromic acid anodising for the structural bonding of aluminium alloys. *Int. J. Adhes. Adhes.* **26**, 419–453 (2006).
6. Yendall, K. A. & Critchlow, G. W. Novel methods, incorporating pre- and post-anodising steps, for the replacement of the Bengough–Stuart chromic acid anodising process in structural bonding applications. *Int. J. Adhes. Adhes.* **29**, 503–508 (2009).
7. Kollek, H. Some aspects of chemistry in adhesion on anodized aluminium. *Int. J. Adhes. Adhes.* **5**, 75–80 (1985).
8. Packham, D. in *Handbook of Adhesion Technology* (eds da Silva, L. F. M., Öchsner, A. & Adams, R. D.) Ch. 2 (Springer, 2011).
9. Brockmann, W., Hennemann, O. D., Kollek, H. & Matz, C. Adhesion in bonded aluminium joints for aircraft construction. *Int. J. Adhes. Adhes.* **6**, 115 (1986).
10. Abrahami, S. T., Hauffman, T., de Kok, J. M. M., Mol, J. M. C. & Terryn, H. Effect of anodic aluminum oxide chemistry on adhesive bonding of Epoxy. *J. Phys. Chem. C* **120**, 19670–19677 (2016).
11. Schneider, M., Kremmer, K., Weidmann, S. K. & Fürbeth, W. Interplay between parameter variation and oxide structure of a modified PAA process. *Surf. Interface Anal.* **45**, 1503–1509 (2013).
12. Abrahami, S. T., Hauffman, T., de Kok, J. M. M., Mol, J. M. C. & Terryn, H. XPS analysis of the surface chemistry and interfacial bonding of barrier-type Cr(VI)-free anodic oxides. *J. Phys. Chem. C* **119**, 19967–19975 (2015).
13. McCafferty, E. & Wightman, J. P. Determination of the concentration of surface hydroxyl groups on metal oxide films by a quantitative XPS method. *Surf. Interface Anal.* **26**, 549–564 (1998).
14. Hart-Smith, L. J. A peel-type durability test coupon to assess interfaces in bonded, co-bonded, and co-cured composite structures. *Int. J. Adhes. Adhes.* **19**, 181–191 (1999).
15. Posner, R., Ozcan, O. & Grundmeier, G. in *Design of Adhesive Joints Under Humid Conditions* (eds da Silva, L. F. M. & Sato, C.) Ch. 2 (Springer, 2013).
16. Keller, F., Hunter, M. S. & Robinson, D. L. Structural features of oxide coatings on aluminum. *J. Electrochem. Soc.* **100**, 411–419 (1953).
17. Wood, G. C. & O'Sullivan, J. P. The anodizing of aluminium in sulphate solutions. *Electrochim. Acta* **15**, 1865–1876 (1970).
18. Rider, A. N. & Arnott, D. R. The influence of adherend topography on the fracture toughness of aluminium-epoxy adhesive joints in humid environments. *J. Adhes.* **75**, 203–228 (2001).
19. Underhill, P. R. & Rider, A. N. Hydrated oxide film growth on aluminium alloys immersed in warm water. *Surf. Coat. Technol.* **192**, 199–207 (2005).
20. Kinloch, A. J., Little, M. S. G. & Watts, J. F. The role of the interphase in the environmental failure of adhesive joints. *Acta Mater.* **48**, 4543–4553 (2000).
21. Venables, J. D., McNamara, D. K., Chen, J. M., Sun, T. S. & Hopping, R. L. Oxide morphologies on aluminum prepared for adhesive bonding. *Appl. Surf. Sci.* **3**, 88–98 (1979).
22. Ye, J., Yin, Q. & Zhou, Y. Superhydrophilicity of anodic aluminum oxide films: From “honeycomb” to “bird’s nest”. *Thin. Solid. Films.* **517**, 6012–6015 (2009).
23. Jeong, C. & Choi, C.-H. Single-step direct fabrication of pillar-on-pore hybrid nanostructures in anodizing aluminum for superior superhydrophobic efficiency. *ACS Appl. Mater. Interfaces* **4**, 842–848 (2012).
24. ASTM Standard D3167-03a. *Standard Test Method for Floating Roller Peel Resistance of Adhesives* (ASTM International, 2003).



Open Access This article is licensed under a Creative Commons Attribution 4.0 International License, which permits use, sharing, adaptation, distribution and reproduction in any medium or format, as long as you give appropriate credit to the original author(s) and the source, provide a link to the Creative Commons license, and indicate if changes were made. The images or other third party material in this article are included in the article's Creative Commons license, unless indicated otherwise in a credit line to the material. If material is not included in the article's Creative Commons license and your intended use is not permitted by statutory regulation or exceeds the permitted use, you will need to obtain permission directly from the copyright holder. To view a copy of this license, visit <http://creativecommons.org/licenses/by/4.0/>.

© The Author(s) 2017